Science of the Total Environment 912 (2024) 169204

Contents lists available at ScienceDirect

Science of the Total Environment

journal homepage: www.elsevier.com/locate/scitotenv

# Optimizing an airborne mass-balance methodology for accurate emission rate quantification of industrial facilities: A case study of industrial facilities in South Korea

Gracie Wong [a], Hui Wang [a], Minwoo Park [b], Jinsoo Park [c,*], Joon-Young Ahn [c], Minyoung Sung [c], Jinsoo Choi [c], Taehyun Park [d], Jihee Ban [d], Seokwon Kang [d], Taehyoung Lee [d], Jongho Kim [e], Beom-Keun Seo [e], Jeong-Hun Yu [e], Jeongho Kim [f], Jung-Hun Woo [b,g,**], Saewung Kim [a]

[a] Department of Earth Systems Science, University of California, Irvine, Irvine, CA, United States
[b] Department of Advanced Technology Fusion, Konkuk University, Seoul, South Korea
[c] Air Quality Research Division, National Institute of Environmental Research, Incheon, South Korea
[d] Department of Environmental Science, Hankuk University of Foreign Studies, Yongin, South Korea
[e] Environmental Research Center, Hanseo University, Seosan-si, South Korea
[f] APM Engineering Co. Ltd., Bucheon-si, South Korea
[g] Department of Civil and Environmental Engineering, Konkuk University, Seoul, South Korea

## HIGHLIGHTS

- We present a comprehensive uncertainty analysis for top-down emission constraints for trace gases from large point sources with an example of $SO_2$.
- The uncertainty analysis illustrates that top-down emission constraints from well-performed airborne observations result in an uncertainty of 20 %.
- The previously reported top-down emission constraints may have an uncertainty of more than 200 %.
- This study provides a quantitative basis to interpret top-down emission constraints from airborne observations.

## GRAPHICAL ABSTRACT

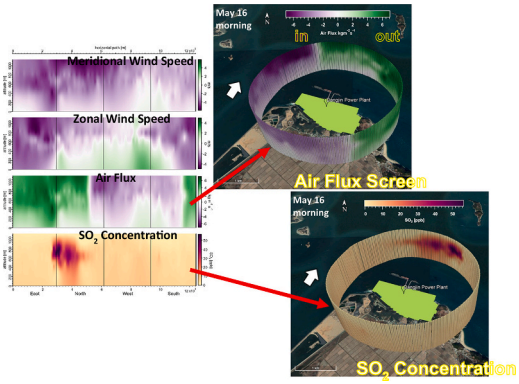


## ARTICLE INFO

Editor: Philip K. Hopke

## ABSTRACT

Accurate estimation of emissions from industrial point sources is crucial in understanding the effectiveness of reduction efforts and establishing reliable emission inventories. In this study, we employ an airborne Chemical Ionization Mass Spectrometry (CIMS) instrument to quantify sulfur dioxide ($SO_2$) emissions from prominent industrial facilities in South Korea, including power plants, a steel mill, and a petrochemical facility. Our analysis utilizes the box mass balance technique to derive $SO_2$ emissions and associated uncertainty. We evaluate the interpolation methods between 2D kriging and 3D radial basis function. The results demonstrate that the total

* Corresponding author.
** Correspondence to: J.H. Woo, Department of Advanced Technology Fusion, Konkuk University, Seoul, South Korea.
*E-mail addresses:* airchemi@korea.kr (J. Park), jwoo@konkuk.ac.kr (J.-H. Woo).

https://doi.org/10.1016/j.scitotenv.2023.169204
Received 7 September 2023; Received in revised form 3 December 2023; Accepted 6 December 2023
Available online 15 December 2023

uncertainty of the box mass balance technique ranges from 5 % to 28 %, with an average of 20 %. Mixing ratio ground extrapolation from the lowest altitude of the airborne sampling to the ground emerges as the dominant source of uncertainty, followed by the determination of the boundary layer height. Adequate sampling at multiple altitudes is found to be essential in reducing the overall uncertainty by capturing the full extent of the plume. Furthermore, we assess the uncertainty of the single-height transect mass balance method commonly employed in previous studies. Our findings reveal an average precision of 47 % for this method, with the potential for overestimating emissions by up to 206 %. Samplings at fewer altitudes or with larger altitude gaps increase the risk of under-sampling and elevate method uncertainties. Therefore, this study provides a quantitative basis to evaluate previously airborne observational emission constraints.

## 1. Introduction

Reliable quantification of the magnitude and uncertainty of trace gas emissions enables accurate modeling of the spatial and temporal distribution of precursor substances and their resultant photochemical reaction products, such as ozone and aerosols. Regional and global emission inventories are mostly compiled using a bottom-up approach, which requires estimating emissions based on statistical data on activity levels, emission factors, and the effectiveness of emission abatement technologies (Ohara et al., 2007; Zhao et al., 2011). However, due to continuous technological advancements and evolving societal infrastructure, these inventory parameters can swiftly become outdated or fail to capture fugitive emissions adequately. This underscores the pressing need for more robust monitoring systems to address these challenges.

Observationally constrained top-down emission estimates have been used to verify bottom-up emission inventories and models in various temporal and spatial scales (Klimont et al., 2017; Li et al., 2017; Streets et al., 2003; Zhang et al., 2009). These studies have illustrated consistent underestimations in emissions by the existing emission inventories (Hsu et al., 2010; Lavoie et al., 2015; Peischl et al., 2013; Wunch et al., 2009). Atmospheric observations from various platforms, including ground-based, aircraft, and satellite measurements, have been employed to acquire these top-down emission constraints. Differential Optical Absorption Spectroscopy (DOAS) techniques have been utilized to assess the total emissions of $SO_2$ and $NO_2$ from area sources by analyzing spectral data obtained from moving or stationary platforms on the ground (Davis et al., 2019; Frins et al., 2011; Johansson et al., 2014; Johansson et al., 2008). Tower networks combined with inverse plume modeling and atmospheric simulations allow us to quantify temporally averaged regional and city-wide emissions, with the resolution dependent on the density of monitoring towers (Lamb et al., 2016; Lauvaux et al., 2016; Lauvaux et al., 2012). Satellite sensors such as the Ozone Monitoring Instrument (OMI) and the TROPOspheric Monitoring Instrument (TROPOMI) demonstrate potential for long-term monitoring of regional emissions, notably $NO_2$ (Fioletov et al., 2020; Fioletov et al., 2015; Koukouli et al., 2018; Krotkov et al., 2016).

The airborne platform allows us to acquire high-resolution spatial datasets, which can be employed in multiple methodologies to derive instantaneous emission estimates. However, this methodology only captures the emissions at the time of sampling up to a couple of hours at most. One such approach utilizes aircraft observations with the Gaussian plume model. This method estimates emissions by analyzing a measured crosswind plume profile that assumes the dispersion pattern of a Gaussian plume emitted from a source under idealized steady-state conditions (Abdel-Rahman, 2008; Weil and Brower, 1984). The dispersion of the plume is determined by employing Pasquil-Gifford coefficients, which are dispersion coefficients based on source distance and estimated atmospheric stability (Turner, 1970). The Gaussian plume model, being relatively simple and conceptually straightforward, serves as the foundation for standard monitoring models like The American Meteorological Society/Environmental Protection Agency Regulatory Model (AERMOD) and the California Puff Model (CALPUFF). However, due to its assumption of a homogeneous wind field across the entire domain, the model is less suitable for large domains where meteorological conditions are expected to vary, as well as for distances $<$100 m from the source and low wind conditions (Babilotte et al., 2010). Numerous studies have quantified uncertainties of various Gaussian plume model implementations, including comparisons to controlled releases, dispersion coefficient manipulation, and Bayesian estimation, (Caulton et al., 2018; Foster-Wittig et al., 2015; Hosseini and Stockie, 2016).

Using airborne datasets in a mass balance approach offers distinct advantages, particularly when dealing with large and heterogeneous areas where the precise identification or localization of emission sources is challenging. This approach can be effectively employed across various aircraft maneuvering tactics, including upwind and downwind spirals, single-height transects, multi-height screens, and box methods (Table S1).

The single-transect method utilizes single-height transects either downwind of the area in a transect perpendicular to the wind direction to intercept the plume (Heimburger et al., 2017; Karion et al., 2013; Peischl et al., 2016; Ryerson et al., 2001; Trainer et al., 1995; Turnbull et al., 2011), or in a circle encompassing the area (Fried et al., 2020; Hopkins et al., 2009). The underlying assumption is that the mixing ratio remains well-mixed and constant at each altitude from the ground up to the planetary boundary layer (PBL). The average wind speed and direction perpendicular to the flight track are used to calculate the horizontal flux. To evaluate the enhancement in mixing ratio, background concentrations are obtained from a second upwind transect or from the edges of the downwind transect outside the main plume width and subtracted from the plume's mixing ratio. Additionally, ascending, or descending spirals may be performed to obtain the vertical profile of pressure and temperature and determine the height of the planetary boundary layer. It should be noted that the single-transect method relies on the assumptions of steady horizontal wind speed as well as a well-mixed planetary boundary layer. While this method reduces flight time, it comes with uncertainties, with assessments indicating potential uncertainties ranging from 65 % to 100 % (Cambaliza et al., 2014; Turnbull et al., 2011). Adequate planning before conducting research flight is essential, such as ensuring the transect is approximately normal to a consistent wind direction and located sufficiently downwind of the emission source to maintain a vertically constant mixing ratio below the planetary boundary layer.

The multi-height screen method has the aircraft fly in horizontal transects downwind of the source at multiple altitudes to reconstruct a screen where the emissions pass through (Cambaliza et al., 2014; Fiehn et al., 2020; Lavoie et al., 2015; Mays et al., 2009). The structure and mixing ratio of the plume is derived by interpolation between each altitude measured to create a screen. Under the assumption of a steady horizontal wind direction normal to the screen, the horizontal flux of emissions from the source can be determined by a background mole fraction subtracted from the flux through the downwind screen. An average background concentration level is determined from the edges of the horizontal transects past the boundaries of the plume enhancement (Karion et al., 2015), or a background flux can be determined from a second upwind screen. The reported uncertainty of this method varies from 30 to 80 % (Cambaliza et al., 2014; Lavoie et al., 2015; Mays et al.,

2009).

The box mass balance method constructs a boxed polygon or a cylinder encompassing the source area from flights sampling at multiple altitudes (Alfieri et al., 2010; Gordon et al., 2015; Kalthoff et al., 2002; Kim et al., 2022; Tadić et al., 2017). An interpolation method is applied to fill in concentration and wind variables between the flight measurements. Inward and outward fluxes for the area of interest are determined by the wind speed normal to the interpolated screens of the box. The emission rate from the source is determined by the net flux out of the box, thereby considering all fluxes within the area of interest. Consequently, this method has minimal uncertainty. Previous studies have determined an uncertainty of ~26 % for the box model method for methane (Gordon et al., 2015). The key for the application is choosing the appropriate interpolation method. Past studies have interpolated the areas between the measurements on the constructed screen using kriging (Cambaliza et al., 2014; Caulton et al., 2014; Gordon et al., 2015; Mays et al., 2009) or Shepard's function (Alfieri et al., 2010). Cambaliza et al. (2014) also tested a local polynomial regression (LPR) method that fits a multi-order of polynomial regression to each point's immediate neighbors to produce interpolated values. The percent change in emissions for $CO_2$ between kriging and LPR was reported to be up to 28 %.

This study presents a series of research flights to constrain trace gas emissions from significant point sources, such as coal power plants, a steel mill, and a petrochemical industrial facility in the Taean Peninsula, South Korea. The flight track was strategically designed to employ the box mass balance method to constrain instantaneous emission rates. Notably, previous estimations of emissions from the Daesan Petrochemical Facility in this region relied on a single-height mass balance method during the Korea-United States Air Quality field campaign (KORUS-AQ) (Fried et al., 2020). A significant challenge in this study was identifying downwind flight paths that are sufficiently far downwind to accurately represent a well-mixed plume vertically from the facility. An essential assumption for the use of the single-height method is the vertical homogeneity of the sampled concentration throughout the boundary layer. However, due to the considerable size of the facility and the uncertainty regarding the precise locations of the emission sources, determining an appropriate downwind distance of this assumption proved challenging. Previous studies employing the single transect method typically focused on much larger sources, such as entire cities, with sampled distances ranging from approximately 10 to 170 km downwind (Heimburger et al., 2017; Peischl et al., 2016; Ryerson et al., 2001; Turnbull et al., 2011). In contrast, the sampling distances from the facilities in both Fried et al.'s study and the current study are notable shorter, ranging from 2 to 3 km. Given this disparity, while the single-height method may be applicable to larger sources at sufficient downwind distances, it becomes crucial to scrutinize its suitability for more spatially concentrated point sources and at closer sampling distances, as undertaken in this study. Ultimately, our study aims to quantitatively assess the current effectiveness of airborne platforms in constraining emission rates, offering valuable insights that refine our understanding of top-down emission constraints reported in prior studies.

## 2. Methods

### 2.1. Airborne observations

A research aircraft, Hanseo B—1900D (HL 5238) has been deployed to airborne science missions since 2019 (Park et al., 2020). The AIMMS-30 (Aircraft Integrated Meteorological Measurement System; Aventech Research Inc., Ontario, Canada) was integrated to quantify meteorological parameters. This system monitors pressure, temperature, relative humidity, three dimensional wind direction and speed, and aircraft location information, including latitude, longitude, heading, rolling, and pitching, with a time resolution of 10 Hz. For this study, we present the 1 Hz averaged dataset to match the time resolution of the other measurements.

A chemical ionization mass spectrometer (CIMS) with the $SF_6^-$ reagent ion is deployed aboard the research aircraft to quantify $SO_2$ (1 Hz). The detailed analytical characteristics of the CIMS system on Hanseo B1900D is thoroughly described in Park et al. (2020). An identical system has been used for airborne $SO_2$ quantification on the NASA DC-8 aircraft since 2004 (Kim et al., 2007). During the research flight, frequent background checks and standard additions were conducted. The background signal is assessed by scrubbed ambient air through a charcoal scrubber for a one-minute duration. An $SO_2$ standard mixture (1 ppm $N_2$ balanced MESA Gas, Santa Ana, CA, U.S.A.) is added to the background flow at 3–5 ppb for the calibration signal for about 1 min. Calibration is interpolated across the full flight time to determine in-flight sensitivity. The sensitivity of the CIMS to $SO_2$ was determined from 249 in-flight calibrations to be 4 Hz $ppt^{-1}$. The uncertainty of the $SO_2$ measurement is derived from the uncertainty of the $SO_2$ standard gas, mass flow controller, and the precision (1σ) of the in-flight calibrations. The uncertainty of the gas cylinder was ±5 %, and typical accuracy of the mass flow controller (MKS, model 1179) was ±1.0 %. The precision of 249 calibrations obtained for all flights is 7 %. The estimated measurement uncertainty of the $SO_2$ measurement is 9 %. The limit of detection (LOD) for $SO_2$ is derived from three standard deviations (3 σ) of in-flight background signals and in-flight sensitivity. Typical LOD for $SO_2$ is ~40 ppt over 1 s.

The Taean region is located on the west coast of South Korea. It includes Taean powerplant, Daesan Petrochemical Facility, Dangjin powerplant, Hyundai Steel Mill, and Boryung Powerplant located approximately at sea level (Fig. 1). The surrounding landscape consists mostly of cropland and forests. Taean powerplant has a facility area of ~1.5 $km^2$ with ten chimney stacks at heights of 150 m. Dangjin powerplant has a facility area of ~1.8 $km^2$ encompassing eight chimney stacks with a height of 150 m and two stacks at 208 m. In 2018, Dangjin and Taean power plants were in the world's top 5 power plants in power generation capability (Grant et al., 2021). Daesan Petrochemical Facility, which is approximately 16 $km^2$, comprises separate plants spread across the entire area. Emissions for Daesan Petrochemical have been estimated using a single-height mass balance method and Korean National Emission Inventory (clean air policy support system, CAPSS) during the Korea-United States Air Quality field campaign (KORUS-AQ) (Fried et al., 2020). Hyundai Steel Mill has a facility area of ~7.5 $km^2$ with three sintering furnaces at the height of 150 m, three coke ovens, and two blast furnaces. Boryung powerplant has a facility area of ~1 $km^2$ and includes eight stacks at 150 m and two stacks at 65 m from coal-burning furnaces.

For the research flights conducted in this study, the typical flight tracks followed vertically stacked transects covering each industrial facility at around seven altitudes ranging from 400 m to 1000 m. We selected eight example flights for analysis, ensuring that the captured $SO_2$ enhancements were adequately represented within the sampled flight altitudes, as summarized in Table 1. The flights were chosen based on several criteria, including the availability of multiple sampling altitudes, the presence of directionally consistent winds throughout the sampling period, and visual inspection confirmed that most of the plume enhancement fell within the sampled altitudes as observed from the interpolated mixing ratio screen.

### 2.2. Mass balance algorithm

The box mass balance approach relies on the principle of mass conservation and the divergence theorem, which states that emissions can be determined by integrating the mass flux across the surfaces of a virtual box that encompasses the facility. This mass flux across the box surfaces is assumed to originate from a fixed control volume within the box. In this study, we employ a modified version of the top-down emission rate retrieval algorithm (TERRA) proposed by Gordon et al. (2015). This algorithm allows us to estimate the total emission rate ($E_C$) according to the following equation:

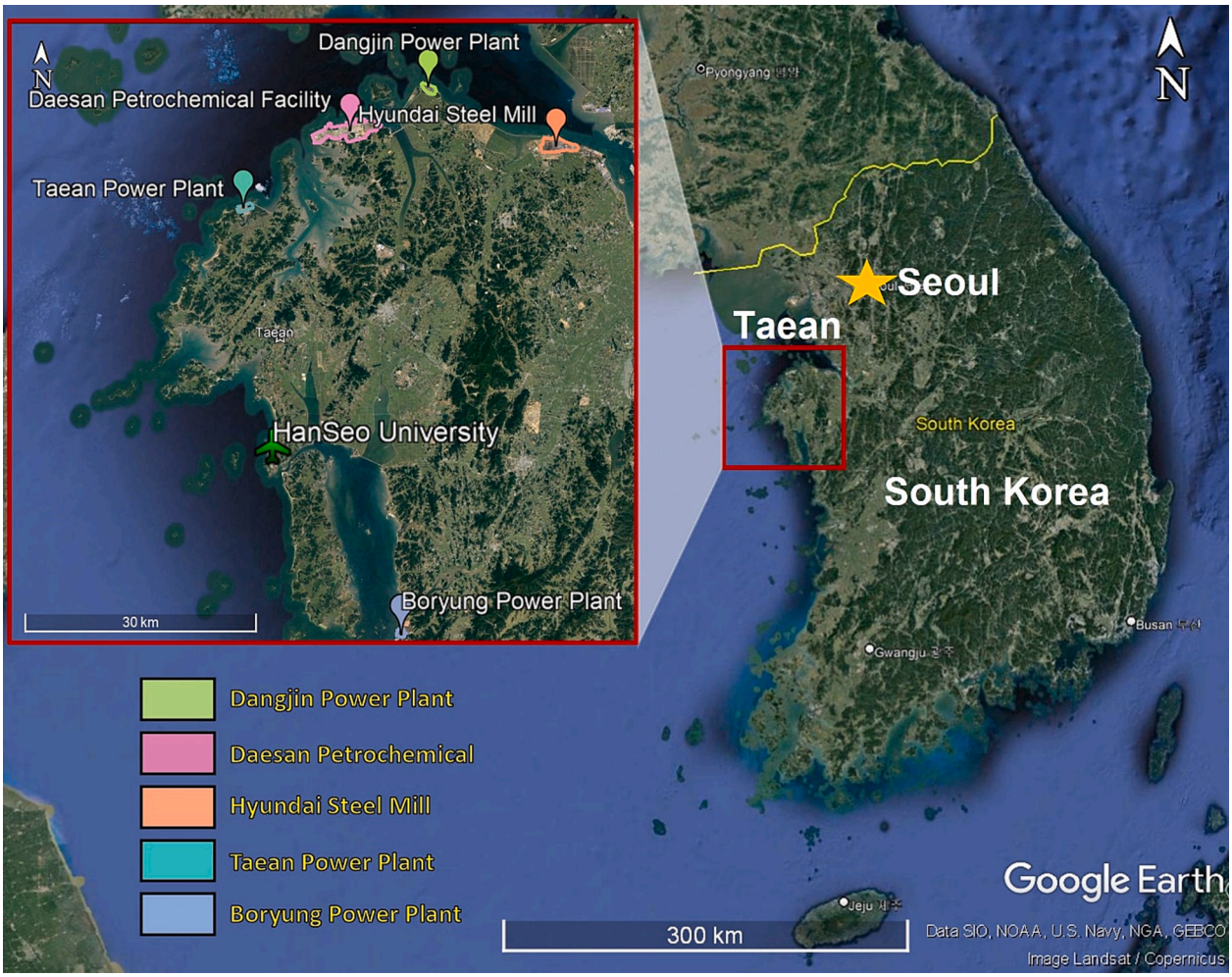


**Fig. 1.** Map of industrial facilities sampled during the aircraft campaign in Taean, South Korea. Map images provided by Data SIO, NOAA, US Navy, NGA, GEBCO, and Google Earth.

**Table 1**
Flight examples presented in this study. The facility size is based on the largest length and width of the facility rounded to the nearest whole kilometer.

| Flight # | F01 | F02 | F03 | F04 | F05 | F06 | F07 | F08 |
|---|---|---|---|---|---|---|---|---|
| Date | 10/27/20 | 10/31/20 | 11/4/20 | 12/9/20 | 12/17/20 | 05/29/21 | 06/01/21 | 07/01/21 |
| Facility name | Taean | Hyundai | Taean | Taean | Hyundai | Dangjin | Daesan | Boryung |
| Facility type | Power plant | Steel Mill | Power plant | Power plant | Steel Mill | Power plant | Petro chemical Facility | Power plant |
| Start time (KST) | 14:21:01 | 12:31:43 | 14:59:47 | 13:58:51 | 12:58:06 | 10:34:00 | 10:53:35 | 08:26:57 |
| End time (KST) | 14:47:32 | 13:07:21 | 15:23:45 | 14:14:58 | 13:32:58 | 11:08:24 | 11:37:08 | 08:51:45 |
| Facility size (km) | 2 × 1 km | 5 × 2 km | 2 × 1 km | 2 × 1 km | 5 × 2 km | 2 × 1 km | 9 × 3 km | 1 × 1 km |
| Distance from facility (km) | 1.8 | 2.3 | 1.8 | 1.5 | 2.5 | 2 | 2.5 | 2.5 |
| Average wind speed (m/s) | 3.4 | 7.1 | 5.8 | 2.7 | 6.2 | 7.3 | 6.3 | 4.7 |
| Wind direction | NW (296°) | SW (216°) | NW (331°) | NW (339°) | NW (313°) | NW (293°) | SW (218°) | SE (102°) |

$$Ec = E_{C,H} + E_{C,V} - E_{C,X} + E_{V,D} \quad (1)$$

where $E_{C,\,H}$ is the horizontal advective flux through the lateral walls of the box, $E_{C,\,V}$ is the flux through the top ceiling of the box, $E_{C,\,X}$ is the change in mass due to chemical conversion of the compound within the box, and $E_{V,\,D}$ is the compound emission deposition to the ground surface.

The aircraft trajectories are not perfectly stacked at each altitude due to wind interferences and the aircraft maneuvering contributing to a certain degree of deviation of the tracks. Therefore, a reference flight path is determined to represent the overall horizontal component of the screen that encompasses the facility (Fig. S1b). To capture the center of the plume adequately, the reference flight path is manually determined based on the density of measurements at a horizontal location and from a central transect where the maximum $SO_2$ concentration is observed. The lateral walls of the box are constructed from the reference path up to the boundary layer height as a two-dimensional screen wrapped around the facility. The start of the horizontal path length ($s$) of the reference flight path is visually set as the southeast corner of the shape and progresses counterclockwise. The path length is calculated in meters as a function of the longitude ($x$) and latitude ($y$).

The measured mixing ratios, zonal wind ($U$), meridional wind ($V$), and air density are interpolated to fill areas on the screen and extrapolated to the ground to a resolution of 40 × 20 m ($s \times z$). 3D interpolation uses a radial basis function with weights estimated by the multiquadric function. Each observation point within 500 m of the determined

reference path is included in the interpolation. The air flux through the screen is calculated as a function of zonal wind, meridional wind, and air density as

$$\iint \rho_{air} U_{\perp} ds dz \tag{2}$$

Air density ($\rho_{air}$) is calculated from the measured temperature ($T$), pressure ($p$), and % relative humidity ($RH$) as (Rogers and Yau, 1996):

$$\rho_{air} = \frac{p}{RT\left(1 + 0.6\chi_{H_2 0}\right)}, \chi_{H_2 0} = \frac{A_d \varepsilon}{p} exp\left(\frac{T_d}{B_d}\right) \tag{3}$$

where $R = 287.1$ J kg$^{-1}$ K$^{-1}$; $\chi_{H2O}$ is the water vapor mixing ratio; $A_d = 3.41 \times 109$ kPa; $\varepsilon = 0.622$; $B_d = 5420$ K; and $T_d$ is the dew-point temperature calculated from the August-Roche-Magnus approximation

$$T_d(T, RH) = \frac{\lambda\left(ln\left(\frac{RH}{100}\right) + \frac{\beta T}{\lambda + T}\right)}{\beta - \left(ln\left(\frac{RH}{100}\right) + \frac{\beta T}{\lambda + T}\right)} \tag{4}$$

where $\lambda = 243.12$ °C; °$\beta = 17.62$.

The wind speed normal to the path ($U_{\perp}$) *is* calculated as

$$U_{\perp} = \frac{V\frac{ds}{dx} - U\frac{ds}{dy}}{\sqrt{\left(\frac{ds}{dx}\right)^2 + \left(\frac{ds}{dy}\right)^2}} \tag{5}$$

The mixing ratios of the compounds are interpolated for each point on the screen and combined with the air flux to calculate the emission rate of the compounds using the following equation:

$$E_c = M_R \iint \chi_C \rho_{air} U_{\perp} ds dz \tag{6}$$

where $\chi_C$ is the mixing ratio of the species and $M_R$ is the ratio of the compound molar mass over the molar mass of air (64.066/28.97 for $SO_2$). The sign of the normal wind is used to determine flux in vs flux out of the area enclosed by the screen, with a positive sign representing flux out of the box. The final emission rate EC is determined by assessing the net flux in and out of the box's walls. Consequently, this final emission rate exclusively captures emissions originating within the box's volume, where the point source facility of interest is located. Hence, this approach can be extended to species with high background levels.

### 2.3. Interpolation and extrapolation techniques

Previous mass balance studies have used a 2D kriging approach to interpolate the screen (Cambaliza et al., 2014; Gordon et al., 2015; Mays et al., 2009). We compare the 2D kriging approach to a 2D and 3D radial basis function (RBF) interpolation. Kriging is a semi-parametric approach that considers the spatial structure of the data by fitting a semivariogram to model the variance between points based on their distance (Chiles and Delfiner, 2012). For a 2D interpolation, each observation is mapped to the closest point on the screen with the exact value observed. Therefore, the interpolation relies on a 2D distance between points on the screen to determine weights without considering the distance from the emission sources. Past studies have commonly observed sources at a larger scale (city-wide, clusters of industrial facilities, agricultural regions) with transect lengths from 5 to 150 km (Table S1). In these cases, the uncertainty associated with these flight track deviations is likely relatively low (Cambaliza et al., 2014; Gordon et al., 2015). As the spatial scale of the examples in this study is smaller than those of the previous studies, we expect this simplification to cause more uncertainty.

A radial basis function defines its value by the distance between the input and a reference point. Commonly used radial basis functions include the Gaussian and Multiquadric function. The chosen function affects how nearby data points contribute to the interpolated value at a specific location. Radial basis function interpolation is a non-parametric approach to interpolate data ($x$) using the weighted sum of radial basis functions:

$$C_i(x_i) = w_1 f(x_i, x_1) + w_2 f(x_i, x_2) + \ldots + w_n f(x_i, x_n) \tag{7}$$

where $C$ is the concentration, $w_i$ are the weights, and $f$ is the chosen radial basis function. Weights are assigned by solving the equation using the known data points (Buhmann, 2000). RBF allows for interpolation throughout a non-stationary surface where the spatial structure varies depending on the sampling location. Considering the 3D distance of the observations to the horizontal screen allows for a 3D interpolation. Here, we perform a 2D and 3D interpolation of the horizontal screen of the box using the radial basis function with the multiquadric activation function from the Python package scipy.interpolate.Rbf (Virtanen et al., 2020). When the more conventionally used kriging approach is expanded to 3 dimensions (pykrige.ok3d.OrdinaryKriging3D), the model calculations for our number of observations are time-consuming and limited by computational storage capacity. RBF as a surrogate model is significantly more computationally efficient due to using neural networks to determine weights rather than a parameterized 3D semivariogram (Bagheri et al., 2017).

The lowest altitude flown is ~400 m for each flight due to flight regulations, resulting in a lack of measurements from 400 m to the ground. The ground elevation under the flight path is taken from SRTM1 database by National Aeronautics and Space Administration (Farr et al., 2007; NASA JPL, 2013). It is projected onto the walls of the mixing ratio and air flux box to serve as the ground elevation for the ground extrapolation discussed in the next section.

The $SO_2$ emission sources for the industrial facilities in our study originate from elevated stacks of ~150 m. As a result, we need to extrapolate the distribution of $SO_2$ concentration from this altitude to the ground to obtain comprehensive emission estimates. To address these contributions, we have adopted a linear constant-to-background scheme. The linear constant-to-background scheme involves fitting a linear relationship between the concentration sampled at the lowest altitude of the screen and a background value at the ground. In this study, we have set the background value to 0 ppb. Additionally, we present two alternative extrapolation results. The first alternative is a constant extrapolation, which assumes that the concentration observed at the lowest sampled altitude remains constant and extends to the ground along the length of the screen. The second alternative is a background extrapolation, which assumes no presence of $SO_2$ below the lowest altitude where samples were taken. Therefore, these two extrapolation methods serve as the upper and lower limit ranges, respectively, for estimating the contribution of $SO_2$ emissions to the ground.

The vertical wind speed distribution is estimated from the lowest sampled altitude to the ground using the logarithmic wind law equation (Blackadar and Tennekes, 1968; Tennekes, 1973).

$$U = \left(\frac{u_*}{\kappa}\right) ln\left(\frac{z - d}{z_0}\right) \tag{7}$$

where $u_*$ is the friction velocity, κ is Von Karman's constant, a nondimensional universal constant determined from observations valued as κ = 0.4 (Foken, 2006; Högström, 1988), $z_0$ is the roughness length where the mean velocity is zero due to roughness of surfaces, and $d$ or zero plane displacement is the height at which the mean velocity is zero due to large obstacles such as buildings and tree canopy. Values for $z_0$ and $d$ are qualitatively determined from visual inspection of the terrain surrounding the industrial facilities on Google Earth. The industrial facilities in this study are all located by the coast. The rest of the surrounding terrain is made up of cropland, forested trees, and buildings related to the facility Assuming a terrain of 60 % open sea, 20 % croplands, 10 % deciduous forests, and 10 % buildings related to major

facilities (Grimmond and Oke, 1999), resulting in the average *z0* value of 0.5 m and the *d* value of 2 m (Oke, 1987).

The friction velocity $u_*$ is calculated using the determined $z_0$ and *d* values and each windspeed value at the lowest altitude sampled along the path. The calculated $u_*$ value is then used to determine the vertical windspeed profile down to the ground altitude for each point (*s*) along the path. Finally, the air density below the measured altitudes of the box is approximated using an exponential fit, described in Table S1.

### 2.4. Flux through the ceiling

To accurately calculate the flux through the top face of the box, it is necessary to have information on concentration and wind values across the entire top face. However, in practice, such data is often limited to the edges of the box. This is due to constraints such as the unknown height of the planetary boundary layer (PBL) before the flight and local flight regulations that restrict flying over the top face. A simplified approach can calculate the flux through the ceiling using the mean concentration, vertical wind speed, and air density along the top edge (Alfieri et al., 2010; Kalthoff et al., 2002). The $SO_2$ flux through the top edge of the screen is calculated as

$$E_{C,V} = A\, M_R \overline{\chi}_{C,top} \overline{\rho}_{air} \overline{w}_{top} \quad (8)$$

where the $w_{top}$ and $\chi_{C,top}$ are the mean vertical windspeed and mixing ratio at the top edge of the screen and *A* is the top area of the box. In our examples, this flux contributes up to 7 % of the total $SO_2$ emission.

## 3. Results and discussion

### 3.1. Comparative analysis of interpolation methods: radial basis function and kriging

The computational results for the interpolations of $SO_2$ and air flux fields are presented in Table 2, along with calculated $SO_2$ emission rates from 2D interpolation with kriging and RBF, and 3D interpolation with RBF. The 2D and 3D RBF interpolation results are compared to the kriging results to highlight the difference between the type of interpolation (kriging vs RBF) and dimensions considered (2D vs. 3D), respectively. In addition to the estimated $SO_2$ emissions, correlation statistics among three different methods are also presented in Table 3.

The interpolation results between kriging and 2D RBF fall within the methodological uncertainty with high $R^2$ values (>0.945) and consistent emission estimates (<3 %) except flight F06. The discrepancy in F06 is mainly attributed to the disagreement in air flux interpolation calculations ($R^2 = 0.883$) rather than the $SO_2$ plume interpolation calculations, which demonstrate excellent agreement ($R^2 = 0.999$). The main difference in the meteorological observation between flight F06 and the rest of the flights is that a large number of data points in the lower part of the flight tracks were missing due to technical issues, as illustrated in Fig. 2b-f. The kriging algorithm used in this study employs "simple kriging," assuming a stationary process with a known, constant mean throughout the entire domain. Consequently, the kriging interpolation tends to drift towards the mean of the existing data. This approach poses challenges when applying airborne observation datasets of concentrations and meteorological parameters, as the average of all data points does not adequately capture local variations. This is particularly evident when visually comparing the interpolation results of F06 and F08 (Fig. 2, S15), and is reflected in the relatively lower correlation coefficients ($R^2 = 0.883, 0.945$). In contrast, RBF interpolation employs linear combinations of radial basis functions to approximate the multivariate function, allowing for greater flexibility and smoothing between data points. This provides a more prudent approach with large missing data points.

Excluding this notable outlier (F06), the 2D approach consistently yields similar results regardless of the interpolation method employed. Thus, the disparities observed in the $SO_2$ emission calculations between 2D kriging and 3D RBF can be attributed to including an additional dimension. Given the relative proximity of the presented examples to the emission sources compared to previous studies (e.g., Table s1), it is reasonable to expect that neglecting a spatial scale may lead to more significant differences in interpolation outcomes. Indeed, the discrepancies in $SO_2$ mixing ratio between 2D and 3D interpolation are more substantial compared to those in the air flux field interpolation results. This can be attributed to the fact that there are anticipated variations in $SO_2$ within the 500 m tolerance of the flight track extraction, which likely exceed those of the meteorological parameters used for air flux calculations. As a result, the $R^2$ values between 2D and 3D $SO_2$ interpolation indicate a weaker agreement compared to the air flux calculations. Notably, F06 stands out as an outlier, exhibiting the lowest correlation coefficient ($R^2$) in $SO_2$ interpolation and the largest difference in air flux interpolation. The systematic difference is caused by the condensed nature of the plumes, which only can be accurately interpolated with the consideration of all spatial dimensions. In summary, the consideration of all spatial dimensions is a prudent approach. To investigate further on uncertainty from different approaches in 3D interpolation techniques, we applied different radial basis function such as linear and Gaussian kernels for flux calculations. The results illustrate that there are no statistically relevant differences with the multi-quadric kernel, applied in the presented flux calculations. We attempted to

**Table 2**
Computational results for interpolation by radial basis function and kriging. Emission rates and percent difference are rounded to the nearest integer.

| | F01 | F02 | F03 | F04 | F05 | F06 | F07 | F08 |
|---|---|---|---|---|---|---|---|---|
| Emission rates (kg $hr^{-1}$) | | | | | | | | |
| Kriging | 550 | 600 | 192 | 571 | 1424 | 333 | 1413 | 641 |
| 2D Radial Basis Function | 549 | 599 | 196 | 583 | 1434 | 291 | 1415 | 659 |
| 3D Radial Basis function | 566 | 729 | 242 | 592 | 1558 | 518 | 1433 | 563 |
| | | | | | | | | |
| 2D Kriging vs 2D RBF | | | | | | | | |
| $SO_2$ emission % change | 1 | 0 | 2 | 2 | 1 | 13 | 0 | 3 |
| $SO_2$ slope | 0.993 | 1.010 | 1.024 | 1.006 | 1.009 | 1.003 | 1.005 | 0.997 |
| $SO_2$ $R^2$ | 0.987 | 0.997 | 0.990 | 0.996 | 0.982 | 0.999 | 0.998 | 0.990 |
| air flux slope | 1.003 | 0.997 | 0.994 | 1.004 | 1.005 | 0.829 | 0.978 | 0.912 |
| air flux $R^2$ | 0.998 | 0.999 | 0.997 | 0.996 | 0.995 | 0.883 | 0.989 | 0.945 |
| | | | | | | | | |
| 2D Kriging vs 3D RBF | | | | | | | | |
| $SO_2$ emission % change | 3 | 19 | 23 | 4 | 9 | 43 | 1 | 13 |
| $SO_2$ slope | 0.871 | 1.012 | 1.042 | 0.986 | 0.970 | 1.108 | 1.057 | 0.841 |
| $SO_2$ $R^2$ | 0.797 | 0.649 | 0.847 | 0.835 | 0.889 | 0.772 | 0.822 | 0.852 |
| air flux slope | 0.991 | 0.981 | 0.952 | 0.947 | 0.988 | 0.832 | 0.969 | 0.890 |
| air flux $R^2$ | 0.975 | 0.965 | 0.960 | 0.951 | 0.980 | 0.886 | 0.972 | 0.918 |

**Table 3**
Emission rates calculated based on varying mixing ratio ground extrapolation methods. Mixing ratio ground extrapolation methods include constant, background, and linear constant-background extrapolations. The linear constant-background ground extrapolation method is considered the base case for our examples where $SO_2$ emissions originate from elevated stacks. The uncertainty due to ground extrapolation technique is determined as the percent change of a constant or background extrapolation from the base case. Constant extrapolation emission is considered the upper-limit range and background extrapolation emission is a lower-limit range for the ground extrapolation uncertainty.

| Flight # | F01 | F02 | F03 | F04 | F05 | F06 | F07 | F08 |
|---|---|---|---|---|---|---|---|---|
| Constant (kg $hr^{-1}$) | 671 | 878 | 296 | 715 | 1940 | 536 | 1820 | 599 |
| Constant-background (kg $hr^{-1}$) | 566 | 729 | 242 | 592 | 1558 | 518 | 1433 | 563 |
| Background (kg $hr^{-1}$) | 444 | 555 | 188 | 444 | 1142 | 497 | 1036 | 527 |
| Constant % change | +18 % | +20 % | +22 % | +21 % | +25 % | +4 % | +27 % | +6 % |
| Background % change | -22 % | −24 % | −22 % | −25 % | −27 % | −4 % | −28 % | −6 % |

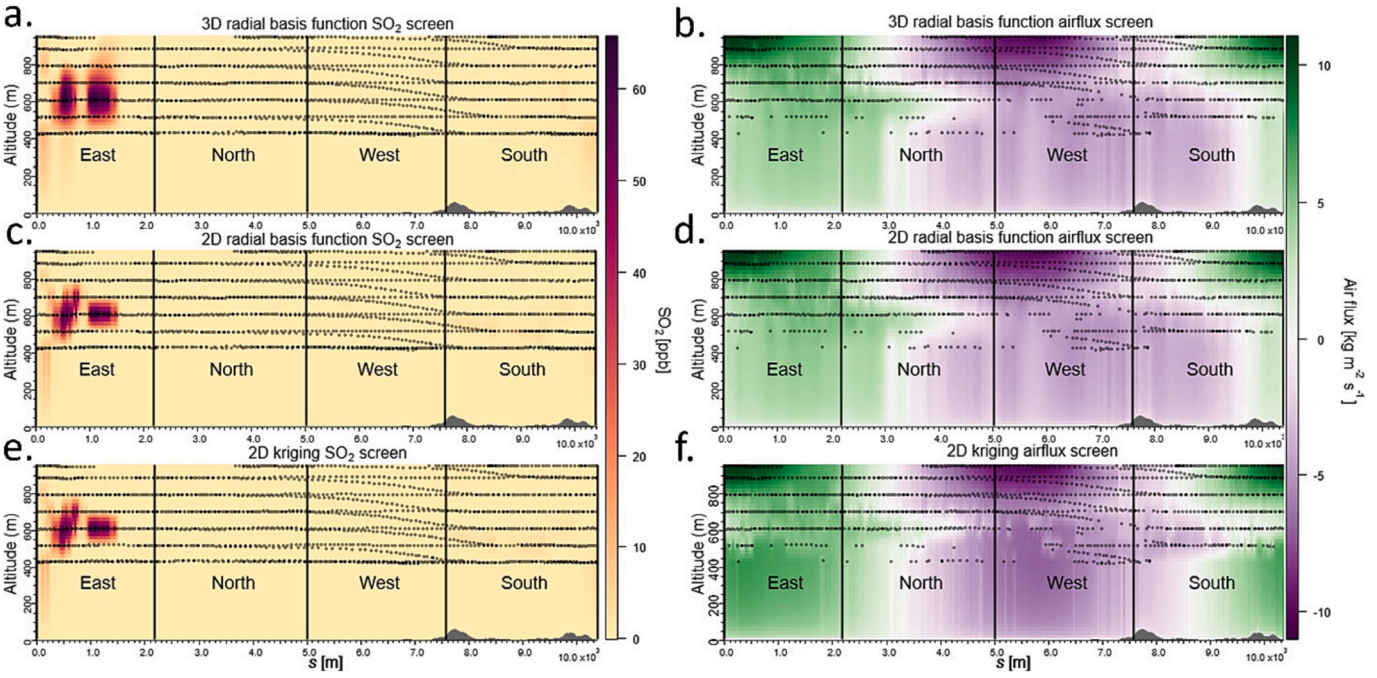


**Fig. 2.** Flight F06 interpolation comparison example. (a) 3D radial basis function interpolated $SO_2$ screen (b) 3D radial basis function interpolation air flux screen (c) 2D radial basis function interpolated $SO_2$ screen (d) 2D radial basis function air flux screen (e) 2D kriging $SO_2$ screen (f) 2D kriging air flux screen. Circle markers denote the location of the measurements used for interpolation.

expand 2D kriging into 3D, which could not be executed with the computational resources within the personal computer configurations.

### 3.2. Uncertainty calculation

The total uncertainty in emission rate for each example is calculated as the root sum square of independent sources of uncertainty in the experimental method. Independent source uncertainties include the mixing ratio ground extrapolation method ($\delta_{Ex}$), wind ground extrapolation ($\delta_{Wind}$), measurement error ($\delta_M$), box-top calculation ($\delta_{Top}$), and box-height selection ($\delta_{BH}$). Total emission rate uncertainty ($\delta$) is calculated as

$$\delta = \sqrt{\delta_{Ex}^2 + \delta_{Wind}^2 + \delta_M^2 + \delta_{Top}^2 + \delta_{BH}^2} \quad (10)$$

To assess the uncertainty arising from ground extrapolation of the mixing ratio, we examine two extreme scenarios: constant extrapolation and background extrapolation, as outlined in Section 2.3.

In the case of powerplant facilities, $SO_2$ is emitted from elevated stacks of approximately 150 m. Given that $SO_2$ is emitted from elevated stacks rather than ground sources in our examples, the constant extrapolation represents a conservative upper-limit emission range. In contrast, the background extrapolation represents a conservative lower-limit emission range. Moreover, our choice of flights to feature in this uncertainty analysis is deliberate, focusing on those where the plumes appear well-captured by the sampled transects, evidenced by the maximum concentration not occurring at the lowest altitude. Hyundai Steel Mill and Daesan Petrochemical Facility are expansive complexes that encompass a more extensive range of industrial activity and $SO_2$ sources, some of which may be emitted from stacks. In contrast, others may originate closer to the ground. Such contributions may need to be characterized by combining with well-conceived ground observations in the future. Nonetheless, the percent change of these extreme cases from the base case (described in Section 2.3) is the uncertainty resulting from the mixing ratio ground extrapolation technique. The findings are presented in Table 3.

In cases where the $SO_2$ plumes remain well within the range of flight altitudes, such as F06 and F09, there is a strong agreement among the three extrapolation techniques, with emission rate differences of <6 %. However, for other cases where a significant portion of the plumes extends beyond the flight altitudes, the differences range up to 28 %. These variations align with the previously anticipated nominal uncertainty range of the methodology employed. This analysis demonstrates that the lowest altitude flown in our study (400 m), allows for the effective containment of most combustion plumes from modern industrial facilities, including coal power plants, steel mills, and petrochemical

manufacturing facilities.

Additional sources of uncertainty, including wind ground extrapolation, measurement error, box-top calculation, and box-height selection, were also explored in the supplementary material. However, their contribution to the total emission rate uncertainty was <1 %. The effects of chemical transformation and deposition were negligible for $SO_2$ at the travel distances from the stack to the flown flight tracks. Several box processes are not considered, such as a change in air mass within the volume, horizontal turbulent flux, and vertical turbulent flux, because the impact of these terms has previously been estimated to contribute well below 1 % to the total emission rate (Alfieri et al., 2010; Gordon et al., 2015; Panitz et al., 2002). The sensitivity of these unconsidered processes to the emission rate is considerably smaller than the uncertainty associated with experimental errors of the method. By neglecting the change in air mass within the volume, it becomes feasible to analyze flights without the need for stationary ground temperature and pressure observations. Additionally, we chose not to include an analysis of the uncertainty associated with storage and release due to changes in wind speed and wind direction during the flight time frame. We justify this decision using the aircraft's instantaneous wind speed and wind direction measurements to calculate air flux around the facility. Each dataset collected for a specific facility spans approximately 30–50 min, and upon reviewing the air flux screens and the average wind speed and wind direction for individual facility flights, we observed minimal variations. Consequently, we assume that the uncertainty related to changes in wind speed and wind direction during our flights is negligible within the sampled time frames. In summary, we conclude that the presented emission estimate framework has an uncertainty of 20 %. The ground extrapolation mostly accounts for the uncertainty.

### 3.3. Examining uncertainty in the single-height approach

We critically examine the single-height transect technique by comparing the emission estimates obtained from each individual altitude transect with our multi-height mass balance estimate. Previous studies employing the mass balance approach have frequently sampled at a single altitude, then assumed a uniform vertical distribution of mixing ratio and wind parameters throughout the boundary layer (Fried et al., 2020; Heimburger et al., 2017; Karion et al., 2013; Peischl et al., 2016; Peischl et al., 2013; Turnbull et al., 2011). However, for our example flights, we observe significant vertical variability in $SO_2$ concentrations, wind speed, and wind direction with the distance from the screen to the significant point sources of the facility ranges from 1 to 8 km. This suggests that transects at multiple altitudes are crucial for accurately characterizing the shape of the plume and air flux for similar industrial point sources and distances. Nevertheless, we acknowledge the need to optimize flight time and resource utilization in such measurements. Hence, it is important to understand the precision and constrain the uncertainties associated with employing a constant vertical profile when only a single-height transect has been observed.

Transects at altitudes with an $SO_2$ enhancement above the background were selected for analysis. A well-mixed boundary layer is assumed with the PBL set at the highest altitude we observed the plume above background levels. The mixing ratio, normal wind speed, pressure, and temperature observed at each transect are applied to every altitude under the PBL. The precision of the single-height transect approach is given by the relative standard deviation of emission estimates determined with each transect.

The results of our analysis, presented in Table 4 and Fig. 3, include emissions calculated using the corresponding multi-transect method for comparison. The precision of the single transect method, represented by the relative standard deviation, ranged from 17 % to 91 %, with an average of 47 %. Compared to the multi-transect approach, many emission estimates obtained from individual transects using the single-transect method showed significant deviations ranging from −79 % to +205 %. These differences were considerably higher than the experimental uncertainty of the multi-transect method, which had a maximum uncertainty of 30 % for our example flights.

**Table 4**
Multi-transect mass balance emission estimates compared with individual single-height transect estimates. The emissions calculated for the single transect method involves using the samples from a single altitude and assuming a well-mixed, vertically constant mixing ratio and wind speed for the entire horizontal walls of the box. The method precision is determined by the relative standard deviation of the emission rates calculated from each individual transect using the single-transect method. The multi-transect approach involves using the samples from all altitudes sampled. Maximum percent change is the change between the individual single-transect method and the multi-transect method.

| Facility # | # of transects | Individual single transects (kg $hr^{-1}$) | Multi-transect (kg $hr^{-1}$) | Max % change | Method precision (%) | PBL (m) |
|---|---|---|---|---|---|---|
| F01 | 6 | 290–887 | 566 | −49 %, +57 % | 41 | 940 |
| F02 | 6 | 153–910 | 729 | −79 %, +25 % | 58 | 940 |
| F03 | 5 | 192–359 | 242 | −21 %, +49 % | 29 | 900 |
| F04 | 5 | 299–856 | 592 | −49 %, +45 % | 35 | 900 |
| F05 | 6 | 733–2049 | 1558 | −53 %, +31 % | 29 | 880 |
| F06 | 3 | 103–1109 | 518 | −80 %, +114 % | 91 | 960 |
| F07 | 6 | 1093–1872 | 1433 | −24 %, +31 % | 17 | 980 |
| F08 | 6 | 228–1722 | 563 | −60 %, +206 % | 73 | 1000 |

The most notable difference in percent change occurred in flight F08, where the single-height transect method varied by up to +206 %, while the multi-transect method had the lowest total uncertainty of 8 %. In this example, the plume was smaller and elevated, and it was sampled at three different altitudes. The assumption of a vertically constant mixing ratio led to a large overestimation of 206 % when the transect at 700 m was used, as the altitude of the maximum concentration was extended vertically to areas with background concentration levels. Conversely, the single-height method underestimated 34 % when the transect at 400 m was used, as a region of lower concentration replaced the higher concentrations of the plume.

### 3.4. Determining optimal altitude sampling requirements

To evaluate the incremental benefit of sampling at additional altitudes, we removed select altitude tracks from the example flights to assess the differences in emission estimates. Our goal was to examine how the emission estimates change when sampling at fewer altitudes by comparing them with the mass balance estimates obtained from approximately seven altitude samplings. For each flight, we conducted four cases: (1) using four altitudes, including the altitude where the maximum concentration was measured, (2) using four altitudes with alternating altitudes between the maximum concentration measurements, (3) using three altitudes, including the altitude with the maximum concentration sampled, and (4) using three altitudes, including the altitude with the lowest concentrations sampled. Including the lowest and highest altitudes measured helped constrain the boundaries of the plume. The standard flight pattern included seven altitudes, sampled every 100 m in altitude. This altitude gap increased to 200 to 300 m for the four and three altitude examples, respectively. The comparison results, with the percent change indicated in parenthesis, are summarized in Fig. 3 and Table 5. The specific transects used for each analysis are presented in the supplement in Figs. S16–23. It is important to note that the calculated emission rates are highly dependent not only

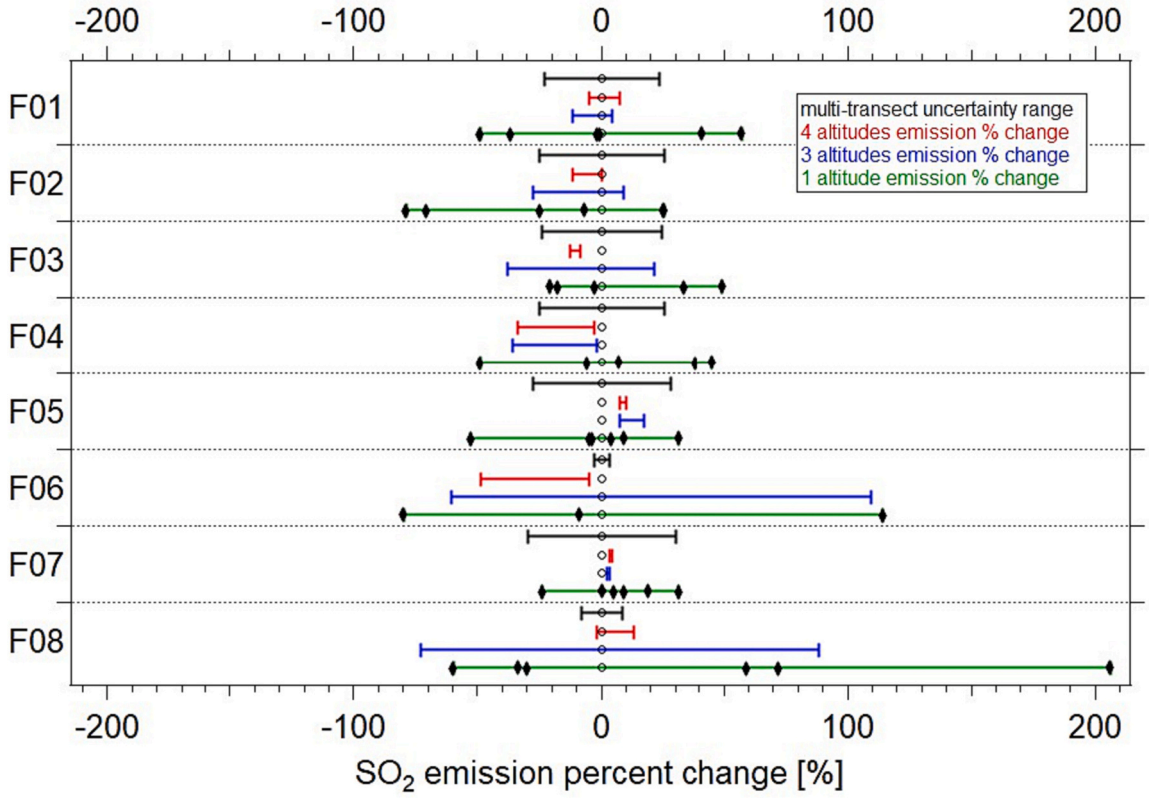


**Fig. 3.** Minimum and maximum emissions percent change calculated using 4 altitudes, 3 altitudes, and 1 altitude examples compared against multi-transect mass balance emissions uncertainty range. Black diamond markers denote the percent change from individual single-height transect calculations.

**Table 5**
Comparison of emission rates from using all altitudes sampled and including only 4 altitudes. Two 4 altitude scenarios are presented: 4 altitudes including the altitude where the maximum concentration was sampled, and 4 altitudes not including the maximum concentration altitude. The lowest and highest altitudes were included in each scenario to constrain the boundaries of the plume. Percent change is determined as the change of the 4 altitudes scenario to the base case of using all altitudes sampled.

| Facility # | All altitudes (kg $hr^{-1}$) | 4 alt. max. (kg $hr^{-1}$) | 4 alt. min. (kg $hr^{-1}$) | 3 alt. max. (kg $hr^{-1}$) | 3 alt. min. (kg $hr^{-1}$) |
|---|---|---|---|---|---|
| F01 | 566 | 606 (+7 %) | 536 (−5 %) | 589 (+4 %) | 496 (−12 %) |
| F02 | 729 | 726 (+0 %) | 645 (−12 %) | 794 (+9 %) | 527 (−28 %) |
| F03 | 242 | 210 (−13 %) | 220 (−9 %) | 293 (+21 %) | 150 (−38 %) |
| F04 | 592 | 577 (−3 %) | 391 (−34 %) | 581 (−2 %) | 379 (−36 %) |
| F05 | 1558 | 1675 (+7 %) | 1708 (+10 %) | 1661 (+7 %) | 1824 (17 %) |
| F06 | 518 | 491 (−5 %) | 263 (−49 %) | 1080 (+109 %) | 203 (−61 %) |
| F07 | 1433 | 1477 (+3 %) | 1492 (+4 %) | 1475 (+3 %) | 1463 (2 %) |
| F08 | 563 | 636 (+13 %) | 552 (−2 %) | 1059 (+88 %) | 153 (−73 %) |

on the number of transects included but also on the variability of the mixing ratio of the transects.

The results demonstrate that the four altitude scenarios generally yield consistent emission estimates within the uncertainty range of the seven altitude examples, except for flight F06. In this example, the plume enhancement was compact and detected only in three altitudes. Therefore, when the four altitudes did not include the altitude with the maximum concentration, it resulted in a percent change of −49 %. For cases where the altitude of the maximum concentration was included, the maximum percent change was only ±13 %, well below the uncertainty of the full multi-transect method of 28 %. Given that the reduction in the number of sampling altitudes from 7 to 4 resulted in a change lower than the overall method uncertainty of 28 %, we deem sampling at 4 altitudes acceptable when estimating the final average emission rate. However, when sampling was reduced to three altitudes, the maximum percent change increased to +109 %. Sampling at fewer altitudes inherently carries the risk of significantly misrepresenting the plume if the altitude with the maximum concentration is not included. Based on this analysis, we recommend that future flights with limited time and resources carefully consider these trade-offs.

### 3.5. Comparative analysis with prior study

The comprehensive examination provides a quantitative basis to evaluate previous top-down emission rate assessments. We provide an uncertainty range for the emission estimates reported in a previous study by Fried et al. (2020). Using the single-height transect method, their study presented $SO_2$ emission estimates from the Daesan Petrochemical Facility during the KORUS-AQ campaign in June 2016. The flights in their study were conducted at a constant altitude of approximately 300 m, with the plumes sampled between 1 and 7 km away from the Daesan facility.

The findings of our analysis prompt us to evaluate previous airborne top-down emission estimates. Our study demonstrates that the pollution plume does not exhibit vertical homogeneity, which is a crucial assumption underlying the single-height transect method. In contrast to other examples, our analysis of the Daesan case (F07) presented in this study reveals $SO_2$ plumes that are more vertically dispersed, primarily due to the presence of multiple stacks at varying heights within the petrochemical facility. Additionally, the Daesan Petrochemical Facility, a larger facility with diverse processes and emissions, exhibits a wider

horizontal spread of plumes that are sometimes distinctly separated. In contrast, power plants typically have concentrated stacks aligned at identical heights, resulting in plumes appearing as one group at the same horizontal locations. Fried et al. (2020) incorporated plume depth up to the calculated mixing layer depth, determined through visual inspection of high-resolution lidar measurements and vertical profiles of the target gaseous compounds. The estimated mixing layer depth was approximately 600 m. Considering that F07 and the KORUS-AQ studies were conducted in June, we would not anticipate significant differences in the assessed plume height between the two. However, in our case, we detected $SO_2$ plumes well above 600 m, up to 1000 m.

In our study, the lowest altitude we sampled around the Daesan facility was 400 m. For the F07 case, the emission flux estimated from the 400 m single-height transect was 1872 kg $hr^{-1}$, representing a 31 % increase compared to the multi-transect method calculation of 1433 kg $hr^{-1}$. We assume that the single-height transect method employed in Fried et al. (2020) resulted in a similar underestimation and apply a correction factor to their reported emission rates (Table 6). It is important to note that the correction factor used is a best-case estimate, assuming that the plumes in both examples exhibit similar vertical distributions.

It is also worth mentioning an attempt to assess top-down $SO_2$ emission from large industrial point sources in the region using the KORUS-AQ dataset (Park et al., 2023). This study integrates the continuous emission monitoring system (CEMS) and single height airborne observational datasets to verify bottom-up emission rates of $SO_2$ and $NO_2$. The outcomes illustrate an acceptable agreement (within 30 %) between top-down and bottom-up emission estimates. Therefore, it may boost a confidence to adapt additional top-down emission estimate methodologies such as the Gaussian plume model if the single-height transect is only available.

## 4. Conclusion

We present a comprehensive quantitative evaluation of how accurate top-down emission constraints can be using airborne observational datasets using an example of $SO_2$. Therefore, we aim to provide the quantitative context to the previously reported top-down emission constraints using airborne observational datasets with various methodologies. This study illustrates that the total uncertainty of the box mass balance technique ranged from 5 % to 28 %, with an average of 20 %, for the presented example flights. The dominant individual source of uncertainty for each flight was attributed to the mixing ratio ground extrapolation, followed by the determination of the box height. This underscores the importance of adequately sampling at multiple altitudes to capture the full extent of the plume and significantly reduce the overall uncertainty.

It is crucial to acknowledge that the uncertainties presented in this study may not encompass all sources that impact the emission rate. Other factors such as vertical and horizontal turbulent fluxes, changes in mass within the box, and uncertainties stemming from the parameterization of the interpolation method could also contribute to the overall uncertainty. Additionally, the study focused on snapshot concentrations of a non-stationary plume, which introduces further complexity and uncertainty due to plume movement during the sampling period. Nonetheless, the uncertainty calculations provided valuable insights for improving future iterations of the mass balance method.

Furthermore, this study evaluated the uncertainty of a single-height transect mass balance method commonly used in previous studies. The analysis demonstrated that this method, which assumes a well-mixed boundary layer and vertically extrapolates the mixing ratio and air flux from the sampled altitude, exhibits an average precision of 47 % and has the potential to overestimate emissions by up to 206 %. This overestimation is primarily attributed to extending regions of maximum observed concentrations vertically to areas with significantly lower enhancements. The uncertainty of the single-height transect method heavily relies on the relative concentration sampled within the transect compared to the rest of the plume. For the studied point sources that emit $SO_2$ from elevated stacks, the observed plumes were not vertically homogeneous between the planetary boundary layer (PBL) and the ground in all flights. Thus, it is recommended that future studies sample at multiple transects beyond the assumed PBL, as resources and time permit, to improve estimation accuracy and reduce uncertainties.

Based on the analysis of the presented flights, it is recommended for future campaigns to sample across a wide altitude range within the PBL. The findings indicate that sampling at least four altitudes in 200-m increments yields reasonable emission estimates. Compared to the emissions calculated using the full set of seven altitudes, the maximum percent change observed was 49 %. Estimates obtained from sampling at three altitudes with larger altitude gaps (300 m) were reasonably similar to estimates including all altitudes, although one example exhibited a difference of 109 %.

The conclusion of this study is not limited to $SO_2$ but can apply to other gases and aerosols emitted from large industrial point sources. In addition, the provided comparison with various top-down emission estimate methodologies can provide the uncertainty ranges of the previously reported top-down emission constraints.

**Table 6**
Reported SO2 emissions from Daesan Petrochemical using the single-height transect method and corrected emissions. Reported emission rates are from KORUS-AQ in 2016 (Fried et al. 2020). Corrected emission rates are based on a single-height transect method overestimation of 31 % determined from this study.

| Dates and plumes | Reported SO2 emission rates [kg $hr^{-1}$] | Correction applied [kg $hr^{-1}$] |
|---|---|---|
| June 2, 2016 | 2358 | 1805 |
| June 3, 2016 | 1343 | 1028 |
| June 3, 2016 | 1188 | 909 |
| June 5, 2016 | 1278 | 978 |
| June 5, 2016 | 1300 | 995 |
| average | 1494 | 1143 |

## CRediT authorship contribution statement

**Gracie Wong:** Writing – review & editing, Writing – original draft, Methodology, Data curation. **Hui Wang:** Writing – review & editing, Writing – original draft, Formal analysis, Conceptualization. **Minwoo Park:** Writing – original draft, Methodology, Investigation, Formal analysis. **Jinsoo Park:** Writing – review & editing, Writing – original draft, Resources, Methodology, Investigation, Funding acquisition. **Joon-Young Ahn:** Writing – original draft, Investigation, Funding acquisition, Formal analysis. **Minyoung Sung:** Writing – original draft, Formal analysis, Data curation. **Jinsoo Choi:** Methodology, Investigation, Formal analysis, Data curation. **Taehyun Park:** Methodology, Investigation, Formal analysis, Data curation. **Jihee Ban:** Methodology, Investigation, Formal analysis, Data curation. **Seokwon Kang:** Methodology, Investigation, Formal analysis, Data curation. **Taehyoung Lee:** Methodology, Investigation, Formal analysis, Data curation. **Beom-Keun Seo:** Methodology, Investigation, Formal analysis, Data curation. **Jeong-Hun Yu:** Investigation, Formal analysis, Data curation. **Jeongho Kim:** Methodology, Investigation, Formal analysis, Data curation. **Jung-Hun Woo:** Writing – review & editing, Writing – original draft, Validation, Supervision, Methodology, Investigation, Formal analysis, Data curation, Conceptualization. **Saewung Kim:** Writing – review & editing, Writing – original draft, Visualization, Validation, Supervision, Resources, Project administration, Methodology, Investigation, Funding acquisition, Formal analysis, Data curation, Conceptualization.

## Declaration of competing interest

The authors have no conflicts of interest to declare. All co-authors

have seen and agree with the manuscript's contents, and there is no financial interest to report. We certify that the submission is original work and is not under review at any other publication.

## Data availability

All data presented in this study is available upon the request to the corresponding authors.

## Acknowledgements

The authors thankfully acknowledge the National Institute of Environmental Research (NIER-2023-01-01-142) of South Korea for funding and logistical support. This research also supported by this research by the National Strategic Project-Fine Particle of the National Research Foundation of Korea (NRF) funded by the Ministry of Science and ICT (MSIT), the Ministry of Environment (ME), and the Ministry of Health and Welfare (MOHW) (2019M3D8A1067406). M.P. and J.W. acknowledge the financial support from Korea Environment Industry & Technology Institute (KEITI) through Climate Change R&D Project for New Climate Regime., funded by Korea Ministry of Environment (MOE). We also appreciate the helpful discussion on the TERRA application generously provided by Andrea Darlington at Environmental Canada and Mark Gordon at York University, Canada.

## Appendix A. Supplementary data

Supplementary data to this article can be found online at https://doi.org/10.1016/j.scitotenv.2023.169204.

## References

Abdel-Rahman, A., 2008. On the Atmospheric Dispersion and Gaussian Plume Model. Proc. 2nd Int. Conf. Waste Manag. Water Pollut. Air Pollut. Indoor Clim. 9.

Alfieri, S., Amato, U., Carfora, M.F., Esposito, M., Magliulo, V., 2010. Quantifying trace gas emissions from composite landscapes: a mass-budget approach with aircraft measurements. Atmos. Environ. 44, 1866–1876. https://doi.org/10.1016/j.atmosenv.2010.02.026.

Babilotte, A., Lagier, T., Fiani, E., Taramini, V., 2010. Fugitive methane emissions from landfills: field comparison of five methods on a French landfill. J. Environ. Eng. 136, 777–784. https://doi.org/10.1061/(ASCE)EE.1943-7870.0000260.

Bagheri, S., Konen, W., Bäck, T., 2017. Comparing Kriging and Radial Basis Function Surrogates 17.

Blackadar, A.K., Tennekes, H., 1968. Asymptotic similarity in neutral Barotropic planetary boundary layers. J. Atmos. Sci. 25, 1015–1020. https://doi.org/10.1175/1520-0469(1968)025<1015:ASINBP>2.0.CO;2.

Buhmann, M.D., 2000. Radial basis functions. Acta Numerica 9, 1–38. https://doi.org/10.1017/S0962492900000015.

Cambaliza, M.O.L., Shepson, P.B., Caulton, D.R., Stirm, B., Samarov, D., Gurney, K.R., Turnbull, J., Davis, K.J., Possolo, A., Karion, A., Sweeney, C., Moser, B., Hendricks, A., Lauvaux, T., Mays, K., Whetstone, J., Huang, J., Razlivanov, I., Miles, N.L., Richardson, S.J., 2014. Assessment of uncertainties of an aircraft-based mass balance approach for quantifying urban greenhouse gas emissions. Atmos. Chem. Phys. 14, 9029–9050. https://doi.org/10.5194/acp-14-9029-2014.

Caulton, D.R., Shepson, P.B., Santoro, R.L., Sparks, J.P., Howarth, R.W., Ingraffea, A.R., Cambaliza, M.O.L., Sweeney, C., Karion, A., Davis, K.J., Stirm, B.H., Montzka, S.A., Miller, B.R., 2014. Toward a better understanding and quantification of methane emissions from shale gas development. Proc. Natl. Acad. Sci. 111, 6237–6242. https://doi.org/10.1073/pnas.1316546111.

Caulton, D.R., Li, Q., Bou-Zeid, E., Fitts, J.P., Golston, L.M., Pan, D., Lu, J., Lane, H.M., Buchholz, B., Guo, X., McSpiritt, J., Wendt, L., Zondlo, M.A., 2018. Quantifying uncertainties from mobile-laboratory-derived emissions of well pads using inverse Gaussian methods. Atmos. Chem. Phys. 18, 15145–15168. https://doi.org/10.5194/acp-18-15145-2018.

Chiles, J.-P., Delfiner, P., 2012. Geostatistics: Modeling Spatial Uncertainty, 2nd, ed. ed. Wiley series in probability and statistics, Wiley, Hoboken, N.J.

Davis, Z.Y.W., Baray, S., McLinden, C.A., Khanbabakhani, A., Fujs, W., Csukat, C., Debosz, J., McLaren, R., 2019. Estimation of $NO_x$ and $SO_2$ emissions from Sarnia, Ontario, using a mobile MAX-DOAS (Multi-AXis Differential Optical Absorption Spectroscopy) and a $NO_x$ analyzer. Atmos. Chem. Phys. 19, 13871–13889. https://doi.org/10.5194/acp-19-13871-2019.

Farr, T.G., Rosen, P.A., Caro, E., Crippen, R., Duren, R., Hensley, S., Kobrick, M., Paller, M., Rodriguez, E., Roth, L., Seal, D., Shaffer, S., Shimada, J., Umland, J., Werner, M., Oskin, M., Burbank, D., Alsdorf, D., 2007. The Shuttle Radar Topography Mission. Rev. Geophys. 45, RG2004. https://doi.org/10.1029/2005RG000183.

Fiehn, A., Kostinek, J., Eckl, M., Klausner, T., Gałkowski, M., Chen, J., Gerbig, C., Röckmann, T., Maazallahi, H., Schmidt, M., Korbeń, P., Nęcki, J., Jagoda, P., Wildmann, N., Mallaun, C., Bun, R., Nickl, A.-L., Jöckel, P., Fix, A., Roiger, A., 2020. Estimating $CH_4$, $CO_2$ and CO emissions from coal mining and industrial activities in the Upper Silesian Coal Basin using an aircraft-based mass balance approach. Atmos. Chem. Phys. 20, 12675–12695. https://doi.org/10.5194/acp-20-12675-2020.

Fioletov, V.E., McLinden, C.A., Krotkov, N., Li, C., 2015. Lifetimes and emissions of $SO_2$ from point sources estimated from OMI. Geophys. Res. Lett. 42, 1969–1976. https://doi.org/10.1002/2015GL063148.

Fioletov, V.E., McLinden, C., Griffin, D., Theys, N., Loyola, D., Hedelt, P., Krotkov, N., Li, C., 2020. Anthropogenic and volcanic point source $SO_2$ emissions derived from TROPOMI onboard Sentinel 5 Precursor: first results. Atmos. Chem. Phys. Discuss. 1–30 https://doi.org/10.5194/acp-2019-1095.

Foken, T., 2006. 50 Years of the Monin–Obukhov Similarity Theory. Bound.-Layer Meteorol. 119, 431–447. https://doi.org/10.1007/s10546-006-9048-6.

Foster-Wittig, T.A., Thoma, E.D., Albertson, J.D., 2015. Estimation of point source fugitive emission rates from a single sensor time series: a conditionally-sampled Gaussian plume reconstruction. Atmos. Environ. 115, 101–109. https://doi.org/10.1016/j.atmosenv.2015.05.042.

Fried, A., Walega, J., Weibring, P., Richter, D., Simpson, I.J., Blake, D.R., Blake, N.J., Meinardi, S., Barletta, B., Hughes, S.C., Crawford, J.H., Diskin, G., Barrick, J., Hair, J., Fenn, M., Wisthaler, A., Mikoviny, T., Woo, J.-H., Park, M., Kim, Jinseok, Min, K.-E., Jeong, S., Wennberg, P.O., Kim, M.J., Crounse, J.D., Teng, A.P., Bennett, R., Yang-Martin, M., Shook, M.A., Huey, G., Tanner, D., Knote, C., Kim, JongHo, Park, R., Brune, W., 2020. Airborne formaldehyde and volatile organic compound measurements over the Daesan petrochemical complex on Korea's northwest coast during the Korea-United States Air Quality study: Estimation of emission fluxes and effects on air quality 28.

Frins, E., Ibrahim, O., Casaballe, N., Osorio, M., Arismendi, F., Wagner, T., Platt, U., 2011. Ground based measurements of SO $_2$ and NO $_2$ emissions from the oil refinery "la Teja" in Montevideo city. J. Phys. Conf. Ser. 274, 012083 https://doi.org/10.1088/1742-6596/274/1/012083.

Gordon, M., Li, S.M., Staebler, R., Darlington, A., Hayden, K., O'Brien, J., Wolde, M., 2015. Determining air pollutant emission rates based on mass balance using airborne measurement data over the Alberta oil sands operations. Atmos. Meas. Tech. 8, 3745–3765. https://doi.org/10.5194/amt-8-3745-2015.

Grant, D., Zelinka, D., Mitova, S., 2021. Reducing $CO_2$ Emissions by Targeting the world's Hyper-Polluting Power Plants.

Grimmond, C.S.B., Oke, T.R., 1999. Aerodynamic properties of urban areas derived from analysis of surface form. J. Appl. Meteorol. 38, 1262–1292. https://doi.org/10.1175/1520-0450(1999)038<1262:APOUAD>2.0.CO;2.

Heimburger, A.M.F., Harvey, R.M., Shepson, P.B., Stirm, B.H., Gore, C., Turnbull, J., Cambaliza, M.O.L., Salmon, O.E., Kerlo, A.-E.M., Lavoie, T.N., Davis, K.J., Lauvaux, T., Karion, A., Sweeney, C., Brewer, W.A., Hardesty, R.M., Gurney, K.R., 2017. Assessing the optimized precision of the aircraft mass balance method for measurement of urban greenhouse gas emission rates through averaging. Elem. Sci. Anthr. 5 https://doi.org/10.1525/elementa.134.

Högström, U., 1988. Non-dimensional wind and temperature profiles in the atmospheric surface layer: a re-evaluation. Bound.-Layer Meteorol. 42, 55–78. https://doi.org/10.1007/BF00119875.

Hopkins, J.R., Evans, M.J., Lee, J.D., Lewis, A.C., H Marsham, J., McQuaid, J.B., Parker, D.J., Stewart, D.J., Reeves, C.E., Purvis, R.M., 2009. Direct estimates of emissions from the megacity of Lagos. Atmos. Chem. Phys. 9, 8471–8477. https://doi.org/10.5194/acp-9-8471-2009.

Hosseini, B., Stockie, J.M., 2016. Bayesian estimation of airborne fugitive emissions using a Gaussian plume model. Atmos. Environ. 141, 122–138. https://doi.org/10.1016/j.atmosenv.2016.06.046.

Hsu, Y.-K., VanCuren, T., Park, S., Jakober, C., Herner, J., FitzGibbon, M., Blake, D.R., Parrish, D.D., 2010. Methane emissions inventory verification in southern California. Atmos. Environ. 44, 1–7. https://doi.org/10.1016/j.atmosenv.2009.10.002.

Johansson, J.K.E., Mellqvist, J., Samuelsson, J., Offerle, B., Lefer, B., Rappenglück, B., Flynn, J., Yarwood, G., 2014. Emission measurements of alkenes, alkanes, SO2, and NO2 from stationary sources in Southeast Texas over a 5 year period using SOF and mobile DOAS. J. Geophys. Res.-Atmos. 119, 1973–1991. https://doi.org/10.1002/2013JD020485.

Johansson, M., Galle, B., Yu, T., Tang, L., Chen, D., Li, H., Li, J.X., Zhang, Y., 2008. Quantification of total emission of air pollutants from Beijing using mobile mini-DOAS. Atmos. Environ. 42, 6926–6933. https://doi.org/10.1016/j.atmosenv.2008.05.025.

Kalthoff, N., Corsmeier, U., Schmidt, K., Kottmeier, C., Fiedler, F., Habram, M., Slemr, F., 2002. Emissions of the city of Augsburg determined using the mass balance method. Atmos. Environ. 36, 19–31. https://doi.org/10.1016/S1352-2310(02)00215-7.

Karion, A., Sweeney, C., Pétron, G., Frost, G., Michael Hardesty, R., Kofler, J., Miller, B. R., Newberger, T., Wolter, S., Banta, R., Brewer, A., Dlugokencky, E., Lang, P., Montzka, S.A., Schnell, R., Tans, P., Trainer, M., Zamora, R., Conley, S., 2013. Methane emissions estimate from airborne measurements over a western United States natural gas field. Geophys. Res. Lett. 40, 4393–4397. https://doi.org/10.1002/grl.50811.

Karion, A., Sweeney, C., Kort, E.A., Shepson, P.B., Brewer, A., Cambaliza, M., Conley, S. A., Davis, K., Deng, A., Hardesty, M., Herndon, S.C., Lauvaux, T., Lavoie, T., Lyon, D., Newberger, T., Pétron, G., Rella, C., Smith, M., Wolter, S., Yacovitch, T.I., Tans, P., 2015. Aircraft-based estimate of Total methane emissions from the Barnett shale region. Environ. Sci. Technol. 49, 8124–8131. https://doi.org/10.1021/acs.est.5b00217.

Kim, Jeonghwan, Seo, B., Lee, T., Kim, Jongho, Kim, S., Bae, G.-N., Lee, G., 2022. Airborne estimation of SO2 emissions rates from a coal-fired power plant using two

top-down methods: a mass balance model and Gaussian footprint approach. Sci. Total Environ. 855, 158826 https://doi.org/10.1016/j.scitotenv.2022.158826.
Kim, S., Huey, L.G., Stickel, R.E., Tanner, D.J., Crawford, J.H., Olson, J.R., Chen, G., Brune, W.H., Ren, X., Lesher, R., Wooldridge, P.J., Bertram, T.H., Perring, A., Cohen, R.C., Lefer, B.L., Shetter, R.E., Avery, M., Diskin, G., Sokolik, I., 2007. Measurement of $HO_2NO_2$ in the free troposphere during the Intercontinental Chemical Transport Experiment - North America 2004. J. Geophys. Res.-Atmos. 112, 1–10. https://doi.org/10.1029/2006JD007676.
Klimont, Z., Kupiainen, K., Heyes, C., Purohit, P., Cofala, J., Rafaj, P., Borken-Kleefeld, J., Schöpp, W., 2017. Global anthropogenic emissions of particulate matter including black carbon. Atmos. Chem. Phys. 17, 8681–8723. https://doi.org/10.5194/acp-17-8681-2017.
Koukouli, M.E., Theys, N., Ding, J., Zyrichidou, I., Mijling, B., Balis, D., van der A, R.J., 2018. Updated SO<sub>2</sub> emission estimates over China using OMI/Aura observations. Atmos. Meas. Tech. 11, 1817–1832. https://doi.org/10.5194/amt-11-1817-2018.
Krotkov, N.A., McLinden, C.A., Li, C., Lamsal, L.N., Celarier, E.A., Marchenko, S.V., Swartz, W.H., Bucsela, E.J., Joiner, J., Duncan, B.N., Folkert Boersma, K., Pepijn Veefkind, J., Levelt, P.F., Fioletov, V.E., Dickerson, R.R., He, H., Lu, Z., Streets, D.G., 2016. Aura OMI observations of regional $SO_2$ and $NO_2$ pollution changes from 2005 to 2015. Atmos. Chem. Phys. 16 https://doi.org/10.5194/acp-16-4605-2016.
Lamb, B.K., Cambaliza, M.O.L., Davis, K.J., Edburg, S.L., Ferrara, T.W., Floerchinger, C., Heimburger, A.M.F., Herndon, S., Lauvaux, T., Lavoie, T., Lyon, D.R., Miles, N., Prasad, K.R., Richardson, S., Roscioli, J.R., Salmon, O.E., Shepson, P.B., Stirm, B.H., Whetstone, J., 2016. Direct and indirect measurements and modeling of methane emissions in Indianapolis. Indiana. Environ. Sci. Technol. 50, 8910–8917. https://doi.org/10.1021/acs.est.6b01198.
Lauvaux, T., Schuh, A.E., Uliasz, M., Richardson, S., Miles, N., Andrews, A.E., Sweeney, C., Diaz, L.I., Martins, D., Shepson, P.B., Davis, K.J., 2012. Constraining the $CO_2$ budget of the corn belt: exploring uncertainties from the assumptions in a mesoscale inverse system. Atmos. Chem. Phys. 12, 337–354. https://doi.org/10.5194/acp-12-337-2012.
Lauvaux, T., Miles, N.L., Deng, A., Richardson, S.J., Cambaliza, M.O., Davis, K.J., Gaudet, B., Gurney, K.R., Huang, J., O'Keefe, D., Song, Y., Karion, A., Oda, T., Patarasuk, R., Razlivanov, I., Sarmiento, D., Shepson, P., Sweeney, C., Turnbull, J., Wu, K., 2016. High-resolution atmospheric inversion of urban CO2 emissions during the dormant season of the Indianapolis Flux Experiment (INFLUX). J. Geophys. Res.-Atmos. 121, 5213–5236. https://doi.org/10.1002/2015JD024473.
Lavoie, T.N., Shepson, P.B., Cambaliza, M.O.L., Stirm, B.H., Karion, A., Sweeney, C., Yacovitch, T.I., Herndon, S.C., Lan, X., Lyon, D., 2015. Aircraft-based measurements of point source methane emissions in the Barnett Shale Basin. Environ. Sci. Technol. 49, 7904–7913. https://doi.org/10.1021/acs.est.5b00410.
Li, M., Zhang, Q., Kurokawa, J., Woo, J.-H., He, K., Lu, Z., Ohara, T., Song, Y., Streets, D. G., Carmichael, G.R., Cheng, Y., Hong, C., Huo, H., Jiang, X., Kang, S., Liu, F., Su, H., Zheng, B., 2017. MIX: a mosaic Asian anthropogenic emission inventory under the international collaboration framework of the MICS-Asia and HTAP. Atmos. Chem. Phys. 17, 935–963. https://doi.org/10.5194/acp-17-935-2017.
Mays, K.L., Shepson, P.B., Stirm, B.H., Karion, A., Sweeney, C., Gurney, K.R., 2009. Aircraft-based measurements of the carbon footprint of Indianapolis. Environ. Sci. Technol. 43, 7816–7823. https://doi.org/10.1021/es901326b.
NASA JPL, 2013. NASA Shuttle Radar Topography Mission Global 1 Arc Second V003 [Dataset].
Ohara, T., Akimoto, H., Kurokawa, J., Horii, N., Yamaji, K., Yan, X., Hayasaka, T., 2007. An Asian emission inventory of anthropogenic emission sources for the period 1980–2020. Atmos. Chem. Phys. 26.
Oke, T.R., 1987. Boundary Layer Climates. Mathuen & Co Ltd., London, John Wiley, New York. https://doi.org/10.4324/9780203407219.
Panitz, H.J., Nester, K., Fiedler, F., 2002. Mass budget simulation of NOx and CO for the evaluation of calculated emissions for the city of Augsburg (Germany). Atmos. Environ. 36, 33–51. https://doi.org/10.1016/S1352-2310(02)00216-9.
Park, J., Choi, J., Moon, K., Kim, D., Kim, H.-J., Ahn, J., Lee, S., Seo, B.-K., Kim, J., Park, S., Kim, S., 2020. Application of chemical ionization mass spectrometry in airborne $SO_2$ observation on Hanseo Beechcraft 1900 D. Asian J. Atmos. Environ. 14, 10.
Park, M., Hu, H., Kim, Y., Fried, A., Simpson, I.J., Jin, H., Weinheimer, A., Huey, G., Crawford, J., Woo, J.-H., 2023. Evaluation of the emission inventory for large point emission sources in South Korea by applying measured data from the NASA/NIER KORUS-AQ aircraft field campaign. Elem. Sci. Anthr. 11, 00105. https://doi.org/10.1525/elementa.2022.00105.
Peischl, J., Ryerson, T.B., Brioude, J., Aikin, K.C., Andrews, A.E., Atlas, E., Blake, D., Daube, B.C., De Gouw, J.A., Dlugokencky, E., Frost, G.J., Gentner, D.R., Gilman, J.B., Goldstein, A.H., Harley, R.A., Holloway, J.S., Kofler, J., Kuster, W.C., Lang, P.M., Novelli, P.C., Santoni, G.W., Trainer, M., Wofsy, S.C., Parrish, D.D., 2013. Quantifying sources of methane using light alkanes in the Los Angeles basin. California. J. Geophys. Res. Atmos. 118, 4974–4990. https://doi.org/10.1002/jgrd.50413.
Peischl, J., Karion, A., Sweeney, C., Kort, E.A., Smith, M.L., Brandt, A.R., Yeskoo, T., Aikin, K.C., Conley, S.A., Gvakharia, A., Trainer, M., Wolter, S., Ryerson, T.B., 2016. Quantifying atmospheric methane emissions from oil and natural gas production in the Bakken shale region of North Dakota. J. Geophys. Res.-Atmos. 121, 6101–6111. https://doi.org/10.1002/2015JD024631.
Rogers, R.R., Yau, M.K., 1996. A Short Course in Cloud Physics, 3rd ed. Butterworth-Heinemann.
Ryerson, T.B., Trainer, M., Holloway, J.S., Parrish, D.D., Huey, L.G., Sueper, D.T., Frost, G.J., Donnelly, S.G., Schauffler, S., Atlas, E.L., Kuster, W.C., Goldan, P.D., Hübler, G., Meagher, J.F., Fehsenfeld, F.C., 2001. Observations of ozone formation in power plant plumes and implications for ozone control strategies. Science 292, 719–723. https://doi.org/10.1126/science.1058113.
Streets, D.G., Bond, T.C., Carmichael, G.R., Fernandes, S.D., Fu, Q., He, D., Klimont, Z., Nelson, S.M., Tsai, N.Y., Wang, M.Q., Woo, J.H., Yarber, K.F., 2003. An inventory of gaseous and primary aerosol emissions in Asia in the year 2000. J. Geophys. Res.-Atmos. 108 https://doi.org/10.1029/2002jd003093.
Tadić, J.M., Michalak, A.M., Iraci, L., Ilić, V., Biraud, S.C., Feldman, D.R., Bui, T., Johnson, M.S., Loewenstein, M., Jeong, S., Fischer, M.L., Yates, E.L., Ryoo, J.-M., 2017. Elliptic cylinder airborne sampling and geostatistical mass balance approach for quantifying local greenhouse gas emissions. Environ. Sci. Technol. 51, 10012–10021. https://doi.org/10.1021/acs.est.7b03100.
Tennekes, H., 1973. The logarithmic wind profile. J. Atmos. Sci. 30, 234–238. https://doi.org/10.1175/1520-0469(1973)030<0234:TLWP>2.0.CO;2.
Trainer, M., Ridley, B.A., Buhr, M.P., Kok, G., Walega, J., Hübler, G., Parrish, D.D., Fehsenfeld, F.C., 1995. Regional ozone and urban plumes in the southeastern United States: Birmingham, a case study. J. Geophys. Res.-Atmos. 100, 18823–18834. https://doi.org/10.1029/95JD01641.
Turnbull, J.C., Karion, A., Fischer, M.L., Faloona, I., Guilderson, T., Lehman, S.J., Miller, B.R., Miller, J.B., Montzka, S., Sherwood, T., Saripalli, S., Sweeney, C., Tans, P.P., 2011. Assessment of fossil fuel carbon dioxide and other anthropogenic trace gas emissions from airborne measurements over Sacramento, California in spring 2009. Atmos. Chem. Phys. 11, 705–721. https://doi.org/10.5194/acp-11-705-2011.
Turner, D.B., 1970. Workbook of Atmospheric Dispersion. US EPA, Washington, DC.
Virtanen, P., Gommers, R., Oliphant, T.E., Haberland, M., Reddy, T., Cournapeau, D., Burovski, E., Peterson, P., Weckesser, W., Bright, J., van der Walt, S.J., Brett, M., Wilson, J., Millman, K.J., Mayorov, N., Nelson, A.R.J., Jones, E., Kern, R., Larson, E., Carey, C.J., Polat, İ., Feng, Y., Moore, E.W., VanderPlas, J., Laxalde, D., Perktold, J., Cimrman, R., Henriksen, I., Quintero, E.A., Harris, C.R., Archibald, A.M., Ribeiro, A. H., Pedregosa, F., van Mulbregt, P., SciPy 1.0 Contributors, Vijaykumar, A., Bardelli, A.P., Rothberg, A., Hilboll, A., Kloeckner, A., Scopatz, A., Lee, A., Rokem, A., Woods, C.N., Fulton, C., Masson, C., Häggström, C., Fitzgerald, C., Nicholson, D.A., Hagen, D.R., Pasechnik, D.V., Olivetti, E., Martin, E., Wieser, E., Silva, F., Lenders, F., Wilhelm, F., Young, G., Price, G.A., Ingold, G.-L., Allen, G.E., Lee, G.R., Audren, H., Probst, I., Dietrich, J.P., Silterra, J., Webber, J.T., Slavič, J., Nothman, J., Buchner, J., Kulick, J., Schönberger, J.L., de Miranda Cardoso, J.V., Reimer, J., Harrington, J., Rodríguez, J.L.C., Nunez-Iglesias, J., Kuczynski, J., Tritz, K., Thoma, M., Newville, M., Kümmerer, M., Bolingbroke, M., Tartre, M., Pak, M., Smith, N.J., Nowaczyk, N., Shebanov, N., Pavlyk, O., Brodtkorb, P.A., Lee, P., McGibbon, R.T., Feldbauer, R., Lewis, S., Tygier, S., Sievert, S., Vigna, S., Peterson, S., More, S., Pudlik, T., Oshima, T., Pingel, T.J., Robitaille, T.P., Spura, T., Jones, T.R., Cera, T., Leslie, T., Zito, T., Krauss, T., Upadhyay, U., Halchenko, Y.O., Vázquez-Baeza, Y., 2020. SciPy 1.0: fundamental algorithms for scientific computing in Python. Nat. Methods 17, 261–272. https://doi.org/10.1038/s41592-019-0686-2.
Weil, J.C., Brower, R.P., 1984. An updated Gaussian plume model for tall stacks. J. Air Pollut. Control Assoc. 34, 818–827. https://doi.org/10.1080/00022470.1984.10465816.
Wunch, D., Wennberg, P.O., Toon, G.C., Keppel-Aleks, G., Yavin, Y.G., 2009. Emissions of greenhouse gases from a North American megacity. Geophys. Res. Lett. 36 https://doi.org/10.1029/2009GL039825.
Zhang, Q., Streets, D.G., Carmichael, G.R., He, K.B., Huo, H., Kannari, A., Klimont, Z., Park, I.S., Reddy, S., Fu, J.S., Chen, D., Duan, L., Lei, Y., Wang, L.T., Yao, Z.L., 2009. Asian emissions in 2006 for the NASA INTEX-B mission. Atmos. Chem. Phys. 9, 5131–5153. https://doi.org/10.5194/acp-9-5131-2009.
Zhao, Y., Nielsen, C.P., Lei, Y., McElroy, M.B., Hao, J., 2011. Quantifying the uncertainties of a bottom-up emission inventory of anthropogenic atmospheric pollutants in China. Atmos. Chem. Phys. 11, 2295–2308. https://doi.org/10.5194/acp-11-2295-2011.